



Comprehensive Study on the Transport Mechanism of Amorphous Indium-Gallium-Zinc Oxide Transistors

Jae Kyeong Jeong, Hyun-Joong Chung, Yeon-Gon Mo,^z and Hye Dong Kim

Samsung SDI Company, Limited, Corporate Research and Development Center, Yongin-City, Gyeonggi-Do 449-902, Korea

High-performance thin-film transistors (TFTs), in which the channel material consisted of amorphous indium-gallium-zinc oxide (a-IGZO) with a bottom gate architecture, were fabricated for array applications. It was found that the dependence of the field-effect mobility on the channel length was greatly affected by the value of the contact resistance (R_C). A high contact resistance ($R_C W \sim 200 \Omega \text{ cm}$) resulted in a significant drop ($\sim 22.3\%$) in the normalized field-effect mobility for the short channel device ($10 \mu\text{m}$), while contact-limited behavior was hardly seen for the device with a low contact resistance ($R_C W \sim 23 \Omega \text{ cm}$). The difference in the channel length dependence of the field-effect mobility was comprehensively investigated based on the conduction mechanism. The fabricated n-channel a-IGZO TFTs with $W/L = 10/10 \mu\text{m}$ exhibited a field-effect mobility of $12.6 \text{ cm}^2/\text{V s}$, threshold voltage of 4.7 V , on/off ratio of 10^8 , and subthreshold gate swing of 0.56 V/decade . © 2008 The Electrochemical Society. [DOI: 10.1149/1.2972031] All rights reserved.

Manuscript submitted June 2, 2008; revised manuscript received July 28, 2008. Published September 9, 2008.

Active-matrix organic light-emitting diode (AMOLED) displays have drawn more attention as a next-generation flat panel display than active-matrix liquid-crystal displays (AMLCDs) because they are thinner, lighter, faster, and more power efficient than AMLCDs. Conventional polycrystalline Si thin-film transistors (poly-Si TFTs), which are used as a backplane for AMOLED displays due to their high mobility and stability, suffer from the nonuniformity of their mobility and threshold voltage, due to the presence of grain boundaries. To circumvent this problem, complex pixel circuits have to be adopted, which limit the design of a high-resolution panel with a high aperture ratio and cause the TFTs to have a low yield and, thus, high cost.^{1,2} Amorphous silicon (a-Si) TFTs, which are used as switching devices for AMLCDs, have the advantage of uniformity and low fabrication cost. Their low mobility ($1 \text{ cm}^2/\text{V s}$), however, may be insufficient to drive large-area AMOLED displays,³ and their device reliability also shows significant deficiencies.⁴ For example, their threshold voltages are seriously shifted under a constant drain current stress ($> 1 \mu\text{A}$), a problem that is attributed to either the creation of defects in the a-Si:H layer or charge trapping in the gate nitride.

Recently, amorphous indium-gallium-zinc oxide (a-IGZO) TFTs have gained much attention as an attractive alternative to poly-Si TFTs because they provide better uniformity in terms of their device characteristics, including the threshold voltage and mobility, due to their amorphous phase nature, and high mobility is attainable with these devices even in the amorphous phase.⁵⁻⁹ Even though high-performance a-IGZO transistors have been reported by a few groups,⁵⁻⁹ there is still a lack of understanding of their transport mechanisms, such as the carrier charge injection from the contact, the bulk conduction of the a-IGZO semiconductor itself, and the systematic correlation between the channel length (L) scaling and the contact resistance.

In this paper, we report the fabrication of high mobility a-IGZO TFTs with excellent uniformity in their device properties for array applications. It is also shown that the a-IGZO transistors are contact-limited devices. A detailed discussion on the carrier conduction mechanism is given in order to provide information on the contact-limited behavior of the a-IGZO transistors.

Device Fabrication

The n-channel a-IGZO TFT array with a bottom gate structure with an etch stopper was fabricated on a $\text{SiO}_2/\text{glass}$ substrate with a size of $370 \text{ mm} \times 400 \text{ mm}$. Lithographically patterned Mo (200 nm) on the substrate was used as the gate electrode. SiN_x (200 nm) film as a gate dielectric layer was deposited by plasma-

enhanced chemical vapor deposition. Subsequently, the a-IGZO film with a thickness of 50 nm was grown by sputtering, using a polycrystalline InGaZnO target at room temperature. During sputtering, the Ar/O_2 gas mixing ratio, input power density, and chamber pressure for sample A (and B) were 65/35 (and 72/28), radio frequency $1.4 \text{ W}/\text{cm}^2$ (and dc $2.0 \text{ W}/\text{cm}^2$), and 5.0 mTorr (and 3.4 mTorr), respectively. After defining the a-IGZO channel using photolithography and wet etching, an etch-stopper layer was formed and then patterned. Mo source and drain electrodes (300 nm) were formed by sputtering, defined by photolithography, and then patterned by dry etching. Finally, the sample was subjected to thermal annealing at 250°C for 1 h. In order to study the current conduction mechanism, parallel devices with the structure of electrode/a-IGZO/electrode were also fabricated. MoW sputtered on a $\text{SiO}_2/\text{glass}$ substrate with a surface area of $50 \text{ mm} \times 50 \text{ mm}$ was used as the bottom electrode. Then, a-IGZO films were fabricated with the two sputtering conditions mentioned above. The indium zinc oxide (IZO) top electrodes, which had a circular shape with a diameter of $200 \mu\text{m}$ and thickness of 200 nm , were deposited by sputtering in the same chamber. The resistivity of the deposited IZO was $8 \times 10^{-4} \Omega \text{ cm}$, as measured by a four-point probe, which was at least three orders of magnitude smaller than that of a-IGZO. Therefore, the voltage drop within the IZO electrode was negligible. The transfer characteristics of the a-IGZO TFTs were measured at room temperature with an Agilent 4156C precision semiconductor parameter analyzer.

Results and Discussion

Contact-limited behavior of a-IGZO TFT.— Figure 1 shows the representative transfer characteristics of the a-IGZO TFTs. The standard deviations of the electrical parameters associated with the performance of the transistors were determined by the evaluation of nine points on one panel. Device A with the a-IGZO channel, which was not optimized, exhibited the field-effect mobility (μ_{FE}) of $2.82 \text{ cm}^2/\text{V s}$, the subthreshold swing (SS) of 0.87 V/decade , and $I_{\text{on/off}}$ ratio of $\sim 10^7$, as shown in Fig. 1c. Device B, with an optimized channel, showed the reasonable μ_{FE} of $12.6 \text{ cm}^2/\text{V s}$, the improved SS of 0.56 V/decade , and a high $I_{\text{on/off}}$ ratio of 10^8 (see Fig. 1b and c), which are much better than those of the a-Si TFT. The lower μ_{FE} and higher SS for device A indicate that the density of state of the IGZO channel material for device A is larger than that for device B. Thus, the larger leakage current of device A would come from the increasing trap-assisted tunneling via the larger gap state. We note that chemical and structural analyses on samples A and B did not show a detectable difference in anion composition ratio inductively coupled plasma-mass spectrometry, thin film density (X-ray reflectivity), and film roughness (X-ray reflectivity and

^z E-mail: ygmo@samsung.com

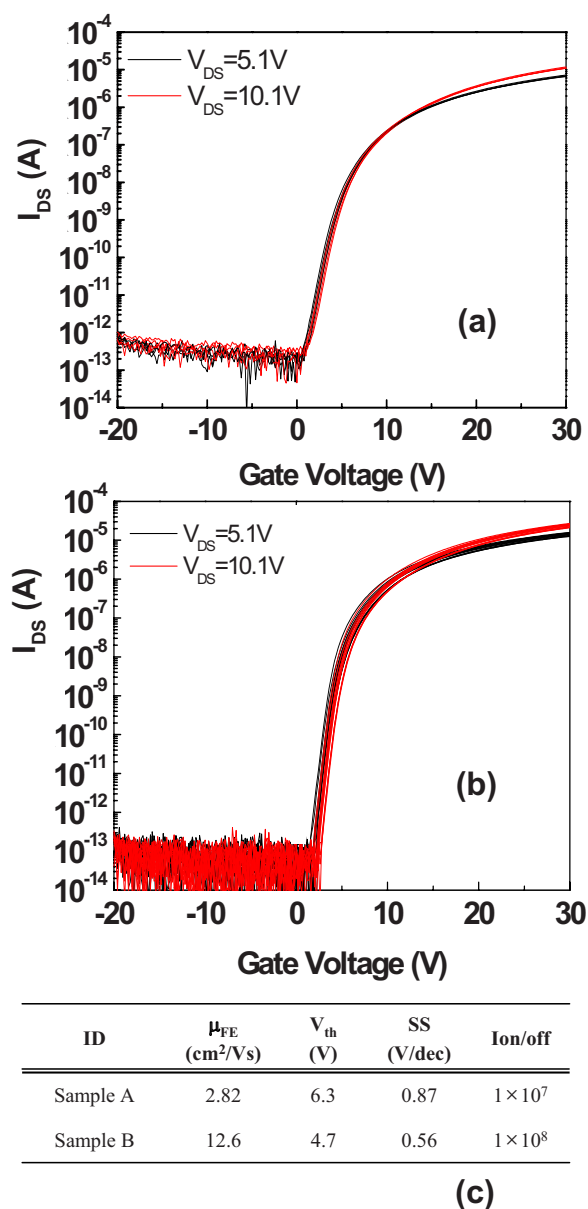


Figure 1. (Color online) Collected transfer characteristics of the a-IGZO TFTs channel width/length (WL), ($W/L = 10 \mu\text{m}/10 \mu\text{m}$) for (a) sample A and (b) sample B. (c) The summaries of device parameters including μ_{FE} , V_{th} , SS, and $I_{on/off}$ ratio for both samples.

atomic force microscopy). One can possibly conjecture that a faster deposition rate of dc sputtering in sample B may result in subtle alleviation on the electrical trap creation.

It is interesting to mention the uniformity of device parameter. The long-range standard deviations ($370 \text{ mm} \times 400 \text{ mm}$) of the threshold voltage (V_{th}) and gate swing for device B were 0.25 V and 0.06 V/decade, respectively. Surprisingly, the short-range uniformity (SRU) of V_{th} was dramatically improved, which is essential for high-quality displays without pixel nonuniformity. The achieved standard deviation of the SRU was $<0.017 \text{ V}$ (not shown), indicating that the very simple pixel circuit consisting of $2Tr + 1Cap$ is sufficient for the high-quality driving of the AMOLED display without any pixel nonuniformity.

Figure 2a shows the dependence of the apparent μ_{FE} on the channel length for device A. The apparent maximum μ_{FE} of the a-IGZO TFTs decreased from 3.63 to 2.82 $\text{cm}^2/\text{V s}$ as the channel length decreased from 50 to 10 μm , as shown in Fig. 2c. However,

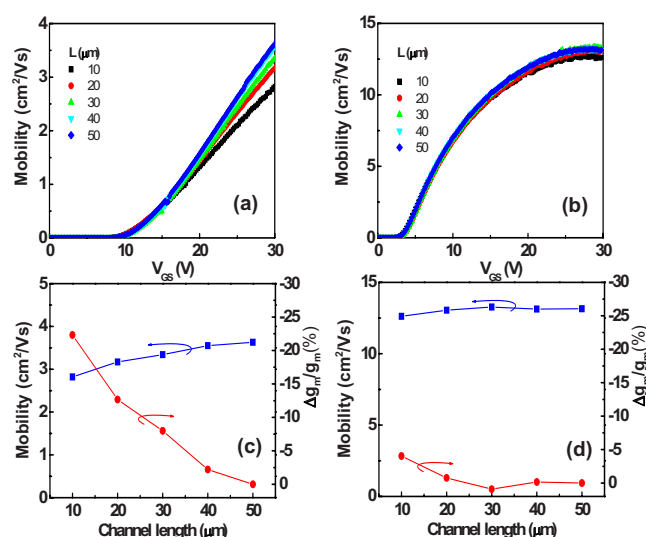


Figure 2. (Color online) Dependence of the apparent field-effect mobility on the channel length of the TFTs with the a-IGZO channel (a) not optimized (sample A) and (b) optimized (sample B), respectively. The variation of maximum apparent field-effect mobility and the drop in the normalized transconductance with respect to the device with $W/L = 10/50 \mu\text{m}$ for (c) sample A and (d) sample B as a function of channel length.

for device B, the apparent field-effect mobility was nearly independent of the channel length of the a-IGZO transistor. The extracted μ_{FE} was $\sim 13.2 \text{ cm}^2/\text{V s}$ for the device with $W/L = 10/10 \mu\text{m}$, having no dependence on the channel length (Fig. 2d). The change in the normalized transconductance more clearly showed the different channel-length dependence for samples A and B. The drop in the transconductance ($\Delta g_m/g_m \times 100\%$) of the 10 μm long device with respect to the device with $W/L = 10/50 \mu\text{m}$ was 22.3% for sample A, whereas it was $<4.0\%$ for sample B, as shown in the inset of Fig. 2c and d.

In fact, it is well known that the apparent μ_{FE} is dependent on the contact resistance (R_C), as follows

$$\mu_{FE} \approx \mu_0 \frac{L}{L + \mu_0 W C_i R_C (V_{GS} - V_T)} \quad [1]$$

where μ_0 and C_i are the true mobility and gate capacitance per unit area, respectively.^{10,11} Assuming that the contact resistance is nearly negligible, the apparent μ_{FE} should be the same as the true mobility and there is no channel-length dependence (sample B). However, if the contact resistance is not negligible, the apparent μ_{FE} should decrease with decreasing channel length (sample A). To verify this hypothesis, we calculated the actual R_C for both devices by determining the device on-resistance (R_{ON}) from the linear region of the transfer curves and plotting the width-normalized value of $R_{ON}W$ as a function of the channel length for different gate voltages.¹²

Figures 3a and b show the width-normalized contact resistance, R_CW , as a function of L at $V_{DS} = 5.1 \text{ V}$ for devices A and B, respectively. The value of R_CW for device A, which is extracted at the y-axis value of crossing point of the extrapolated linear fit of R_CW vs L , was $\sim 200 \Omega \text{ cm}$. It should be noted that typical values of R_CW are ~ 1 and $>1000 \Omega \text{ cm}$ for poly-Si and organic TFTs, respectively.¹³ Indeed, the large contact resistance for device A is responsible for the channel-length dependence of the apparent field-effect mobility. Device B had a much smaller contact resistance ($R_CW \sim 23 \Omega \text{ cm}$). Therefore, it can be concluded that the contact-limited behavior of the a-IGZO transistor comes from the large contact resistance and that the apparent field-effect mobility would be independent of the channel length for the devices with a small contact resistance (for example, $<23 \Omega \text{ cm}$).

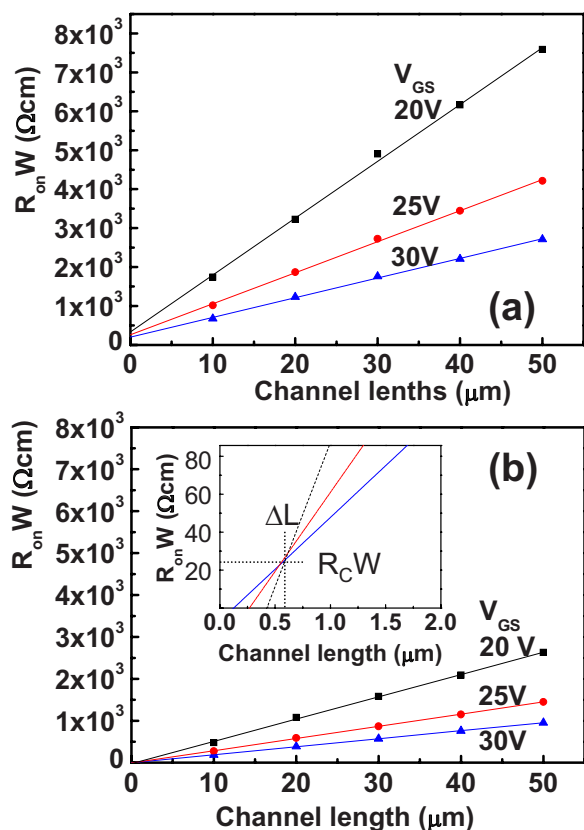


Figure 3. (Color online) The width-normalized device $R_{on}W$ as a function of L at $V_{DS} = 5.1$ V for devices (a) A and (b) B, respectively. The enlarged portion near the crossing point was inserted into the inset of (b). Note that the ΔL (~ 0.59 μm) is the difference between effective channel length and mask-defined channel length. The width-normalized R_C was extracted from the y-axis value of the crossing point for various $R_{on}W$ -vs- L lines.

Understanding of the conduction mechanism.—Next, we discuss the origin of the large contact resistance of the a-IGZO TFTs compared to that of the poly-Si TFTs. In general, the contact resistance is interpreted as the series resistance of the two components: the resistance of the metal/a-IGZO interface ($R_{Injection}$) and the access resistance (R_{Access}) of the a-IGZO film itself from the metal contact to the channel, as shown in Fig. 4. The effective electrical field at the overlapped region between the gate and the source elec-

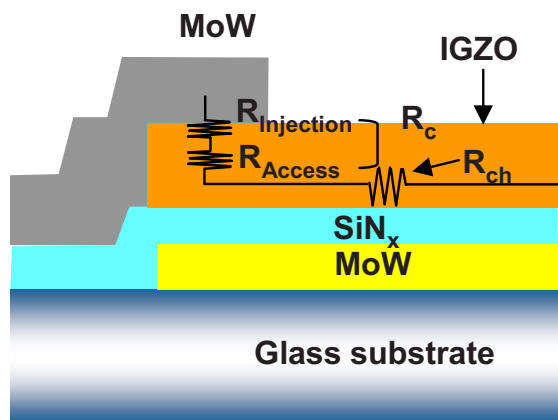


Figure 4. (Color online) Schematic cross-sectional cartoon showing that the contact resistance (R_C) is the summation of the injection resistance ($R_{Injection}$) and access resistance (R_{Access}).

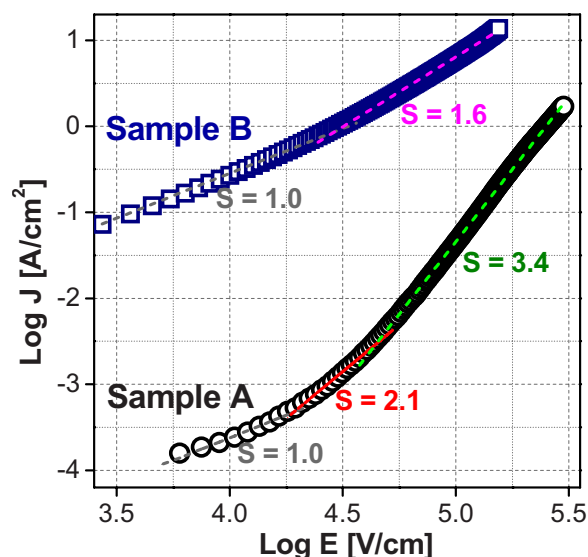


Figure 5. (Color online) $\log J$ vs $\log E$ plots of the metal/a-IGZO/metal samples. The gray S denotes the slope of respective gray lines. See text for details.

trode during the organic light-emitting diode (OLED) device operation can be roughly estimated as follows. During the operation of the OLED for full white gray, the drain current is circa 1 μA for a-IGZO TFTs with a W/L ratio of $10/10$ μm (see Fig. 1). It is quite reasonable to assume that $R_C = 1/2R_S = 1/2R_D$. Because the $R_C W$ values are 200 and 23 Ωcm for samples A and B, respectively (see Fig. 3), the voltage drops caused by the contact resistance, which can be estimated using the relation 1 $\mu\text{A} \times (R_C/2)W/10$ μm , are approximately 0.1 and 0.012 V, respectively. Because the thickness of the active channel is 50 nm, the effective electrical fields for samples A and B are calculated to be around 20 and 2.3 kV/cm, respectively. However, it should be noted that the estimated effective electrical fields (i.e., by dividing the oxide film thickness) is larger than the actual electrical fields because the voltage drops by contact resistance is sustained by the IGZO bulk film itself and the interfacial energy barrier at the metal/IGZO film, which would result in the slight overestimation of the working electrical field. The physical implications of this will be discussed later in conjunction with the conduction mechanism.

In order to determine whether $R_{Injection}$ or R_{Access} is the main contributor to the large contact resistance, the current conduction mechanism in the a-IGZO films was investigated using model devices with an electrode/a-IGZO/electrode structure, which were designed to mimic the carrier injection from the electrode to the a-IGZO channel in TFTs. The large R_C of sample A was found to originate from the bulk a-IGZO itself (R_{Access}) rather than from the interface between the source/drain electrode and the a-IGZO ($R_{Injection}$). The small R_C value of sample B stems from the small value of R_{Access} , and consequently, $R_{Injection}$ plays an important role at a high electric field.

Figure 5 shows the log-log plots of the current density vs electric field [$\log(J)$ vs $\log(E)$] of samples A and B. First of all, the J values of sample B at low (10 kV/cm) and high (100 kV/cm) E are approximately three and two orders of magnitude higher than those of sample A, respectively. This behavior is in qualitative agreement with the higher R_C value of sample A. To understand the current conduction mechanism, the slopes of the log-log plots were analyzed within the framework of the space-charge-limited conduction (SCLC) theory. For sample A, the slope value, S , of the $\log(J)$ vs $\log(E)$ plot increases from 1.0 , to 2.1 to 3.4 as E increases from $E < 20$, to $20 < E < 40$, to $E > 40$ kV/cm, respectively, which is

in agreement with the theory of SCLC with shallow traps, where a transition from ohmic ($J \propto E$), to Mott–Gurney's law ($J \propto E^2$) to a trap-related high-field effect ($S > 2$) is expected with increasing E .^{14–16} For sample B, the S values undergo a gentle increase from 1.0 to 1.6 at $E = 30$ kV/cm. This behavior is not explained by the SCLC framework.

In the presence of a strong E , the charge transport can be enhanced by the Poole–Frenkel effect, which is a lowering of the potential barrier for charge carriers escaping from traps in the presence of an electric field.¹⁴ In addition, the transition from SCLC (bulk limited) to Schottky emission (interface limited) is reported to be a natural phenomenon when the contact is of the accumulation type.^{17,18} To verify these hypotheses, the linear fitting of the $\ln(J/E)$ vs $E^{1/2}$ plot can be used to determine whether the Schottky emission or the Poole–Frenkel effect is the dominating conduction mechanism.^{17,18} The dynamic dielectric constants due to the Schottky emission and Poole–Frenkel mechanisms are extracted from the following equations, respectively

$$\varepsilon_{\text{SC}} = \frac{q^3}{(kTS)^2 4\pi\varepsilon_0} \quad [2]$$

and

$$\varepsilon_{\text{PF}} = \frac{q^3}{(kTS)^2 \pi\varepsilon_0} \quad [3]$$

where S' is the slope of the linear fitting, q is the electronic charge, kT is Boltzmann's constant times the absolute temperature, and ε_0 is the dielectric constant of free space. Note that $\varepsilon_{\text{PF}} = 4\varepsilon_{\text{SC}}$. When the extracted ε_{SC} (or ε_{PF}) values are similar to the high-frequency dielectric constant of a-IGZO, 11.5,¹⁶ for a given range of E , Schottky emission (or Poole–Frenkel mechanism) is likely to be the dominating current conduction mechanism at the given electric field.¹⁹ Another probable high-field effect of bulk-limited conduction, SCLC enhanced by the Frenkel effect (SCL + F), was suggested by Murgatroyd.²⁰ The linear fitting of the $\ln(J/E^2)$ vs $E^{1/2}$ plot enables the possibility of this mechanism occurring to be determined, and the extracted dielectric constant is expressed as

$$\varepsilon_{\text{SCL+F}} = \left(\frac{0.891}{kTS'} \right)^2 \frac{q^3}{\pi\varepsilon_0} \quad [4]$$

where S'' is the slope of the linear fitting.

Figures 6a and b show the $\ln(J/E)$ vs $E^{1/2}$ plots of samples A and B, respectively. From the linear fittings in Fig. 6a, it can be seen that the Poole–Frenkel mechanism dominates the current conduction in sample A when $E > 190$ kV/cm. In addition, the $\ln(J/E^2)$ vs $E^{1/2}$ plot (inset of Fig. 6a) shows that the SCL + F is the limiting mechanism when $40 < E < 180$ kV/cm. Therefore, one can conclude that the current conduction mechanism in sample A undergoes a transition from ohmic, to Mott–Gurney, to SCL + F, to Poole–Frenkel with increasing E . Figure 6b shows that the Schottky emission plays the dominant role in sample B when $30 < E < 150$ kV/cm. Therefore, a transition from ohmic to Schottky emission occurs in sample B with increasing E . Finally, we note that other conduction mechanisms, such as the Fowler–Nordheim tunneling or Hopping conduction theories, did not fit with the current-voltage (I - V) behaviors of samples A and B.

Considering that a-IGZO has a large bandgap (>3.2 eV) and that the free donor concentration of a-IGZO film is $\sim 1 \times 10^{15} \text{ cm}^{-3}$, it is natural to assume that there is a Schottky barrier between the a-IGZO semiconductor and the electrode. Therefore, the observed bulk-limited mechanism (that is, R_{Access} limited) of sample A means that the bulk resistivity is so large that the influence of the Schottky barrier at the electrode/a-IGZO interface is negligible. The bulk resistivity in sample B is so small that the Schottky barrier becomes the dominating factor limiting charge conduction.

As mentioned earlier, the vertical electrical fields at the a-IGZO channel during OLED operation would be ~ 20 and ~ 2.3 kV/cm in

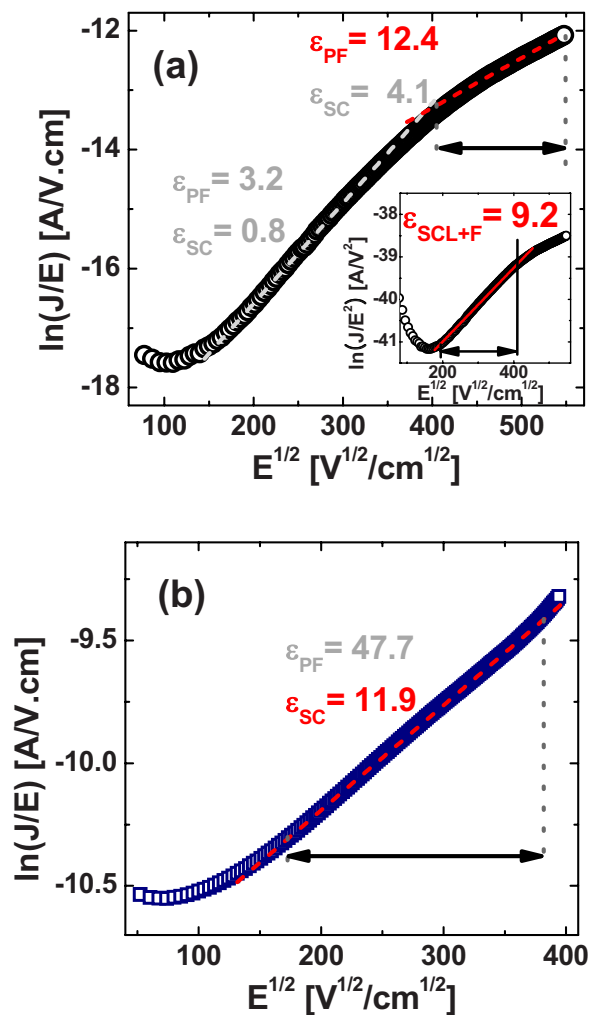


Figure 6. (Color online) The $\ln(J/E)$ vs $E^{1/2}$ plots of (a) sample A and (b) sample B. Inset of sample A is the $\ln(J/E^2)$ vs $E^{1/2}$ plot. ε_{SC} , ε_{PF} , and $\varepsilon_{\text{SCL+F}}$ denote extracted dielectric constants from Schottky emission, Poole–Frenkel, and space-charge-limited conduction enhanced by Frenkel effect mechanisms, respectively, from linear fittings. Black and gray letters denote physically plausible and unlikely conduction mechanisms, respectively. See text for details.

samples A and B, respectively. As shown in Fig. 6, the SCLC conduction mechanism plays an important role in sample A under practical working field condition (~ 20 kV/cm). However, sample B (~ 2.3 kV/cm) is still dominated by ohmic behavior. Now, it is evident that the channel length dependence of the apparent field-effect mobility for device A is due to the relatively high contact resistance, which is reminiscent of the SCLC conduction of a-IGZO film itself from the contact to the channel. Moreover, the channel length-independence of the apparent mobility for device B originated from the ohmic behavior. Therefore, our conclusion is that the reduction of the contact resistance required to fabricate high mobility oxide TFTs and to guarantee the ohmic contact between a-IGZO and the source/drain (S/D) electrode can be achieved by tuning the bulk properties of the a-IGZO film.

In summary, the I/V characteristics of sample A fit well with the framework of the bulk-limited conduction mechanisms. At a low electric field, the SCLC mechanism fits well with the I - V curve, where the conduction is enhanced by the Frenkel effect when a high electric field is applied. This result clearly shows that the current conduction in sample A is bulk limited. Sample B undergoes a transition from ohmic conduction to Schottky emission as the electric

field increases. Thus, for sample B, the electrode/a-IGZO interface plays an important role in limiting the current conduction, because the bulk resistivity is significantly lower than that of sample A.

Conclusion

In summary, it was shown that the channel-length dependence of the apparent field-effect mobility was attributed to the large contact resistance ($>200 \Omega \text{ cm}$ for sample A). As the contact resistance decreased, the channel-length dependence became weaker: in sample B having a much smaller contact resistance ($R_{\text{C}}W \sim 23 \Omega \text{ cm}$), the apparent field-effect mobility was independent of the channel length.

The large contact resistance of sample A originated from the bulk a-IGZO itself (R_{Access}) rather than from the interface between the S/D electrode and the a-IGZO ($R_{\text{Injection}}$). That is, the I - V characteristics of the a-IGZO devices fit well with the framework of the SCLC mechanism. The small contact resistance of sample B stems from the relatively lower R_{Access} compared to that of sample A. Therefore, it is important to make an a-IGZO layer with low resistivity to reduce the value of R_{C} .

The a-IGZO TFT for array applications showed a field-effect mobility of $12.6 \text{ cm}^2/\text{V s}$, threshold voltage of 4.7 V, on/off ratio of 10^8 , and subthreshold slope of 0.56 V/decade, which are much better than those of the a-Si TFT. In addition, the long-range standard deviations of the threshold voltage and gate swing were 0.25 V and 0.06 V/decade, respectively.

Acknowledgments

The authors thank Minkyu Kim, Tae Kyung Ahn, Jong Han Jeong, Hun Jung Lee, Hui Won Yang, and Jin-Seong Park for the fabrication of an a-IGZO TFT array.

Samsung SDI Ltd. assisted in meeting the publication costs of this article.

References

1. J. H. Lee, W. Nam, B. K. Kim, H. S. Choi, Y. M. Ha, and M. K. Han, *IEEE Electron Device Lett.*, **27**, 830 (2006).
2. S. H. Jung, W. J. Nam, and M. K. Han, *IEEE Electron Device Lett.*, **25**, 690 (2004).
3. M. Stewart, R. S. Howell, L. Pires, and M. K. Hatalis, *IEEE Trans. Electron Devices*, **48**, 846 (2001).
4. S. M. Jahinuzzaman, A. Sultana, K. Sakariya, P. Servati, and A. Nathan, *Appl. Phys. Lett.*, **87**, 023502 (2005).
5. K. Nomura, H. Ohta, A. Takagi, T. Kamiya, M. Hirano, and H. Hosono, *Nature (London)*, **432**, 488 (2004).
6. H. Yabuta, M. Sano, K. Abe, T. Aiba, T. Den, H. Kumomi, K. Nomura, T. Kamiya, and H. Hosono, *Appl. Phys. Lett.*, **89**, 112123 (2006).
7. M. Kim, J. H. Jeong, H. J. Lee, T. K. Ahn, H. S. Shin, J.-S. Park, J. K. Jeong, Y.-G. Mo, and H. D. Kim, *Appl. Phys. Lett.*, **90**, 212114 (2007).
8. J.-S. Park, J. K. Jeong, Y.-G. Mo, H. D. Kim, and S.-I. Kim, *Appl. Phys. Lett.*, **90**, 262106 (2007).
9. H. N. Lee, J. W. Kyung, S. K. Kang, D. Y. Kim, M. C. Sung, S. J. Kim, C. N. Kim, H. G. Kim, and S. T. Kim, in *Proceedings of IDW*, pp. 663–666 (2007).
10. D. K. Schroder, *Semiconductor Material and Device Characterization*, 3rd ed., p. 208, John Wiley & Sons, Hoboken, NJ (2006).
11. K. Y. Chan, E. Bunte, H. Stiebig, and D. Knipp, *Appl. Phys. Lett.*, **89**, 203509 (2006).
12. J. Zaumseil, K. W. Baldwin, and J. A. Rogers, *J. Appl. Phys.*, **93**, 6117 (2003).
13. A. Valletta, L. Mariucci, G. Fortunato, and S. D. Brotherton, *Appl. Phys. Lett.*, **82**, 3119 (2003).
14. K. C. Kao and W. Hwang, *Electrical Transport in Solids*, Chap. 2, 3, and 5, Pergamon, New York (1981).
15. F. D. Morrison, P. Zubko, D. J. Jung, J. F. Scott, P. Baxter, M. M. Saad, R. M. Bowman, and J. M. Gregg, *Appl. Phys. Lett.*, **86**, 152903 (2005).
16. H.-J. Chung, J. H. Jeong, T. K. Ahn, H. J. Lee, M. Kim, K. Jun, J.-S. Park, J. K. Jeong, Y.-G. Mo, and H. D. Kim, *Electrochem. Solid-State Lett.*, **11**, H51 (2008).
17. J. G. Simmons, *Phys. Rev. Lett.*, **15**, 967 (1965).
18. C. S. Hwang, *J. Mater. Res.*, **16**, 3476 (2001).
19. W. K. Choi, L. J. Han, and F. L. Loo, *J. Appl. Phys.*, **81**, 276 (1997).
20. P. N. Murgatroyd, *J. Phys. D: Appl. Phys.*, **3**, 151 (1970).